






Skyrmion and skyrmionium formation in the two-dimensional magnet $\text{Cr}_2\text{Ge}_2\text{Te}_6$

L. Powalla ^{1,*},† M. T. Birch ^{2,*},‡ K. Litzius ² S. Wintz ^{2,3} S. Satheesh,¹ M. Weigand,^{2,3} E. Goering,² G. Schütz,² and M. Burghard ¹

¹Max Planck Institute for Solid State Research, Heisenbergstrasse 1, D-70569 Stuttgart, Germany

²Max Planck Institute for Intelligent Systems, Heisenbergstrasse 3, D-70569 Stuttgart, Germany

³Helmholtz-Zentrum Berlin für Materialien und Energie GmbH, Hahn-Meitner-Platz 1, Berlin, D-14109, Germany



(Received 29 June 2023; accepted 7 November 2023; published 15 December 2023)

The recently discovered 2D magnets represent versatile building blocks for spintronic devices. In particular, the out-of-plane 2D ferromagnets Fe_3GeTe_2 and $\text{Cr}_2\text{Ge}_2\text{Te}_6$ (CGT) are attracting strong attention, owing to their ability to host topological spin textures. Among these, CGT is particularly interesting, as its semiconducting property could facilitate electric field control over the spin textures. Here, we systematically explore the magnetic phases of an exfoliated CGT flake with a thickness on the order of 50 nm by scanning transmission x-ray microscopy using three different measurement protocols. The domain periodicity was found to decrease with increasing temperature and decreasing flake thickness, the latter of which can be attributed to the relatively small magnetic anisotropy of CGT. Moreover, the magnetic phase diagram of CGT features a high-temperature skyrmion phase pocket, and skyrmionium formation occurs upon zero-field cooling. The sensitivity of the skyrmions to magnetic field changes indicates that dipolar interactions play a major role in stabilizing these magnetic spin textures.

DOI: [10.1103/PhysRevB.108.214417](https://doi.org/10.1103/PhysRevB.108.214417)

I. INTRODUCTION

The discovery of intrinsic ferromagnetism in van der Waals layered $\text{Cr}_2\text{Ge}_2\text{Te}_6$ (CGT) crystals in 2017 [1] has made a major contribution to establish the still growing research field of 2D magnets, which are highly attractive due to their well defined, atomically flat surfaces and potentially low defect densities [2]. Since then, 2D magnets with long-range order have been intensively studied due to their their fundamental spin physics in low dimensions [3,4], as well as the possibility to tailor their properties via proximity effects in 2D heterostructures [5]. These materials open up novel spintronic applications in the 2D limit such as, e.g., the magnetoelectric spin-orbit (MESO) device, where the magnetic layer is used to store bits of information [6].

Besides simple ferromagnetism, topologically nontrivial spin textures, such as particlelike skyrmions, have been discovered in 2D magnets. In CGT, Lorentz transmission electron microscopy (LTEM) revealed both skyrmions and type-II bubbles, exhibiting mixed chirality and Bloch-type domain walls [7,8]. Such topological spin textures are of strong interest owing to their capability of being manipulated by spin currents or mechanical strain [9,10], which renders

them promising to be implemented into racetracks [11] or 2D neuromorphic computing devices [12]. Moreover, it has been experimentally demonstrated that skyrmions can exist in CGT/ Fe_3GeTe_2 -heterostructures [13], even in the few-layer limit. Further measurements on CGT revealed an anisotropic magnetoresistance [14], and a sizable temperature dependence of the effective magnetic anisotropy [15]. Notably, charge transport studies have revealed a strong gate modulation of the electrical resistance and magnetic anisotropy of exfoliated, few-layer CGT flakes [16–18], achieved through a standard back gate. This property renders CGT potentially useful for electric field control of spin textures. Interestingly, theory has predicted a significant gate tunability for CGT even in the monolayer limit [19].

The details of the formation of skyrmions and the magnetic phase diagram, as well as the formation of different kinds of spin textures in CGT, remain to be explored, to assess their potential as components of 2D spintronic devices. Here, we use scanning transmission x-ray microscopy (STXM) to spatially map the magnetic phases in an exfoliated CGT flake with a thickness between 40 nm and 55 nm, and determine its magnetic phase diagram for three different measurement protocols. Additionally, we observe the formation of skyrmioniums, thus expanding the range of possible 2D magnet hosts for these topological spin textures beyond the previously reported Fe_3GeTe_2 [20]. Our findings underscore that CGT is a promising candidate to host composite skyrmions and control their properties by electrical means.

II. EXPERIMENTAL METHODS

A. Sample preparation

The CGT single crystal was purchased from the company HQ Graphene (The Netherlands). Figure 1(a) reveals the

*These authors contributed equally to this work.

†l.powalla@fkf.mpg.de

‡birch@is.mpg.de

Published by the American Physical Society under the terms of the [Creative Commons Attribution 4.0 International](https://creativecommons.org/licenses/by/4.0/) license. Further distribution of this work must maintain attribution to the author(s) and the published article's title, journal citation, and DOI. Open access publication funded by the Max Planck Society.

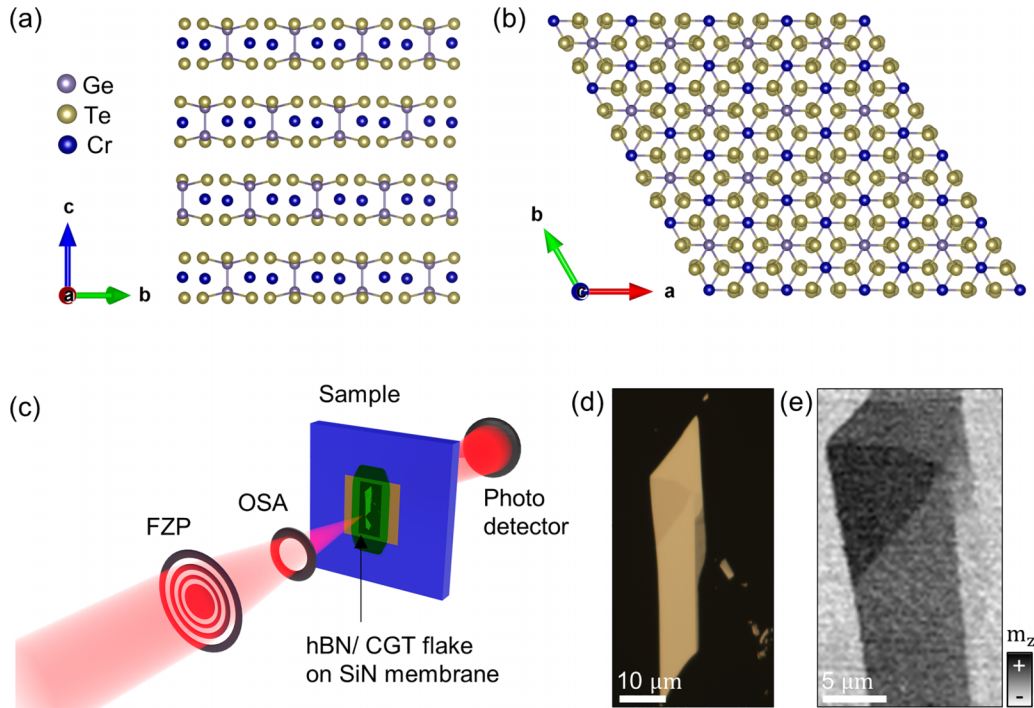


FIG. 1. Crystal structure, optical micrograph, and scanning transmission x-ray microscopy (STXM). (a), (b) Crystal structure of $\text{Cr}_2\text{Ge}_2\text{Te}_6$ in (a) bc projection and (b) ba projection. Data adapted from [21]. (c) Sketch of the STXM measurement setup with Fresnel zone plate (FZP) and order selecting aperture (OSA), sample, and detector. (d) Optical image of the investigated CGT flake, located on a 100 nm thick SiN membrane. (e) XMCD image of the flake acquired at 576.2 eV photon energy at a single polarization of the x-ray photons c^+ obtained by subtracting the images taken at the two magnetic fields ± 250 mT at 47 K. The gray scale indicates the out-of-plane magnetization m_z .

crystalline stacking along the c axis, with the Cr atoms sandwiched in between the layers of Ge and Te atoms, while the hexagonal symmetry of the c projection is displayed in Fig. 1(b). The CGT flake for the STXM experiments was prepared by an all-dry viscoelastic transfer method. In the first step, the CGT bulk crystal was mechanically cleaved and then exfoliated onto a polydimethylsiloxane (PDMS) stamp. A flake with small thickness variations was selected and stamped onto a 100 nm thick Si_3N_4 membrane by controlling the temperature and mechanical forces. Finally, the flake was capped by an exfoliated hexagonal boron nitride (hBN) sheet with a thickness of about 25 nm. A sketch of the sample on the membrane is shown in Fig. 1(c), and an optical microscope image of the flake in Fig. 1(d). The entire process was performed under ambient conditions, with each side of the flake being exposed to atmosphere for approximately 20 min.

B. Magnetic characterization and thickness measurement

Magnetometry measurements were carried out with a quantum design MPMS3 vibrating sample magnetometer. To determine the crystalline axis-dependent magnetic properties, the bulk CGT crystal was aligned along the relevant crystal axis and fixed to a quartz glass rod using GE varnish. A built-in helium cryostat was used to control temperatures down to 4 K, and a magnetic field was applied by a superconducting coil. Atomic force microscopy measurements on the capped flake were performed using a Bruker dimension icon atomic force microscope to determine the thickness of each region. Since the hBN capping renders the thickness evaluation of the

CGT sheet more difficult, the CGT thickness was estimated by averaging over few micrometer long steps.

C. Scanning transmission x-ray microscopy (STXM)

STXM measurements were performed at the UE46 beamline at the BESSY II synchrotron in Berlin with the MAXYMUS x-ray microscope [22]. This technique combines chemical sensitivity, which is enabled by the tunable x-ray source, with a high spatial resolution. Using different polarizations of the x-ray beam (circular right/left), it is possible to extract information about the magnetization originating from a specific atomic species. As illustrated in Fig. 1(c) the x-ray beam of selected photon energy and polarization was focused with the aid of a Fresnel zone plate and an order selecting aperture to a spot size of about 20 nm on the sample plane, resulting in a lateral resolution of approximately 25 nm. Using a piezoelectric stage, the sample was raster scanned through the focused beam at a nominal x-ray energy of 576.2 eV. X-ray magnetic circular dichroism (XMCD), measured with circularly polarized light [23], yields an out-of-plane magnetization contrast of the sample [24]. A He-flow cryostat was used to control the temperature and the applied magnetic field was controlled by varying the arrangement of four permanent magnets. The temperature is measured by a sensor close to the sample. However, we can not exclude a slight temperature difference between the sensor and the sample due to an imperfect thermal coupling. On the L2 and L3 edges, the magnetic contrast is resonantly enhanced due to the match of the photon energy with the atomic absorption edges of the 3d orbitals of Cr. Recording the sample transmission

pixel-by-pixel produces a spatial map of its magnetic structure. The measured signal indicates the out-of-plane magnetization m_z , as exemplified by Fig. 1(e). This kind of STXM technique has been widely used to spatially resolve magnetic states in a range of materials, and has recently been extended to 2D magnets such as FGT [25] and their heterostructures [26]. Note that we represent our data consistently as single helicity STXM images that contain both, structural and magnetic contrast due to better visibility of the magnetic structures in the unprocessed data [27].

We performed imaging according to three different measurement protocols. In the field-sweep (FS) protocol, the magnetic state is initially saturated out-of-plane at a given temperature. The magnetic field is then stepwise changed to opposite magnetic field, while STXM images are acquired after each field step. For the field-cooling (FC) protocol, we cool the sample from above its critical temperature while applying an out-of-plane field. Afterwards, the magnetic field is again stepwise changed to either positive or negative magnetic field, while STXM images are acquired after each field step. For each of the two field sweep directions, an additional field-cooling procedure has to be performed. The zero-field cooling (ZFC) protocol is equivalent to the FC protocol with the difference of achieving the initial state by cooling at nominal zero magnetic field.

III. RESULTS

A. SQUID magnetometry

The magnetic properties of the bulk CGT single crystals were determined using SQUID magnetometry. The hysteresis curves in Figs. 2(a)–2(c), recorded at 5 K, 40 K, and 60 K, respectively, exhibit an out-of-plane easy axis. Figure 2(d) shows the saturation magnetization M_s in dependence of temperature. From temperature-dependent magnetization data at low fields, a critical temperature of 65 K was estimated by extracting the temperature of maximal magnetization gradient (data not shown). This value is in good agreement with the previously reported 61 K [28,29].

The extracted saturation magnetization in Fig. 2(d) features a maximum value of about 168 kA m^{-1} . This value agrees well with that of 159 kA m^{-1} , calculated from the magnetization of $28 \text{ mA m}^2 \text{ g}^{-1}$ reported in [30], using a mass density of 5.68 g cm^{-3} from [31,32]. For estimating the magnetization per Cr atom from the determined saturation magnetization, we use the unit cell volume of 0.83 nm^3 for $\text{Cr}_2\text{Ge}_2\text{Te}_6$, yielding a magnetic moment per unit cell of $15\mu_B$, corresponding to a magnetization of $2.5\mu_B$ per Cr atom, in good agreement with the $2.4\mu_B$ per Cr atom at 5 K reported in [18], and close to the expected high-spin state of the Cr^{3+} ions.

To derive the magnetocrystalline anisotropy from the SQUID data, the work required to magnetize the sample along the in-plane and out-of-plane directions was estimated from the hysteresis loops, via the following integral:

$$W_{H,i} = -1\mu_0 \int_0^{M_s} H dM. \quad (1)$$

The corresponding integrals for in-plane ($W_{H,\parallel}$) and out-of-plane direction ($W_{H,\perp}$) were then used to estimate the effective magnetic anisotropy $K_{\text{eff}} = W_{H,\parallel} - W_{H,\perp}$. Since the measured

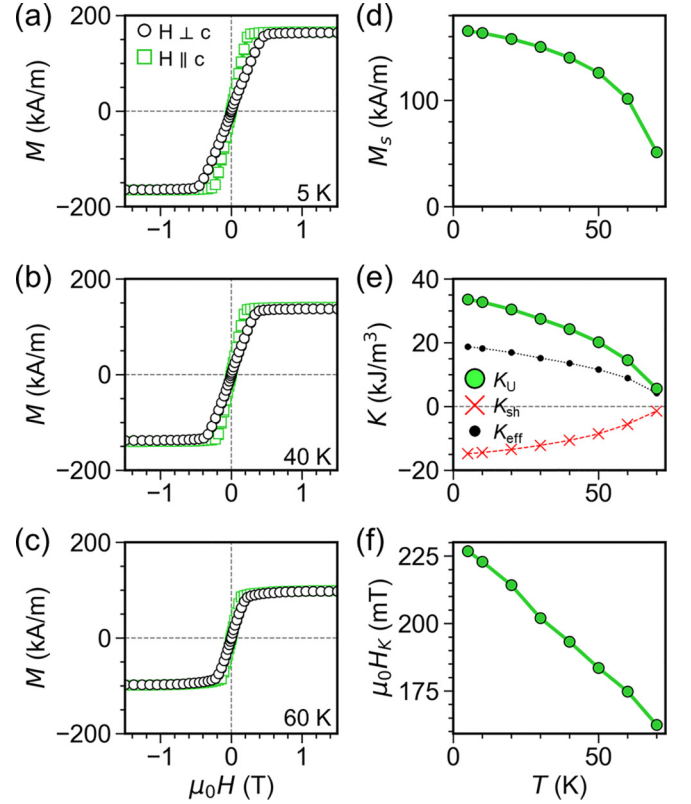


FIG. 2. Bulk sample characterization by SQUID magnetometry. (a)–(c) Hysteresis curves for in-plane and out-of-plane magnetic fields acquired at (a) 5 K, (b) 40 K, and (c) 60 K. (d) Temperature-dependent saturation magnetization. (e) Measured magnetic anisotropy K_{eff} , calculated shape anisotropy K_{sh} , and resulting estimated uniaxial magnetocrystalline anisotropy K_{u} as a function of temperature. (f) Anisotropy field as a function of temperature.

value still includes the shape anisotropy $K_{\text{sh}} = -\frac{1}{2}\mu_0 N_{\text{d}} M_{\text{s}}^2$, the latter needs to be subtracted from the measured K_{eff} to obtain the magnetocrystalline uniaxial anisotropy $K_{\text{u}} = K_{\text{eff}} - K_{\text{sh}}$. For a cuboid sample with a length of $a = b = 2 \text{ mm}$ and a height of $c = 0.1 \text{ mm}$, the anisotropy difference between the in-plane and out-of-plane direction can be approximated by $N_{\text{d}} = N_z - N_x = \frac{a-c}{a+2c} \approx 0.86$, using $N_x = \frac{n}{2n+1}$ and $N_z = \frac{1}{2n+1}$ with $n = \frac{c}{a}$ from [33]. The different magnetic anisotropies (K_{u} , K_{eff} , K_{sh}) are plotted in Fig. 2(e). On this basis, the anisotropy field $H_{\text{k}} = \frac{2K_{\text{u}}}{M_{\text{s}}}$ is obtained. The maximum resulting value of K_{u} of 35 kA m^{-1} is slightly lower than the 47 kA m^{-1} reported in [15]. However, the present ratio of 0.42 between the magnetic anisotropy at 60 K and at 4 K is similar to the reported value of 0.41 [15]. Notably, the magnetic anisotropy of CGT is significantly lower in comparison to other 2D materials, such as CrBr_3 with 86 kA m^{-1} [34], CrI_3 with 301 kA m^{-1} [34], or Fe_3GeTe_2 with up to 500 kA m^{-1} [25]. The weak magnetic anisotropy manifests itself in a rather small anisotropy field of only 220 mT at 5 K and 180 mT at 60 K [see Fig. 2(f)]. Moreover, the linear dependence of the magnetization around zero magnetic field indicates that the bulk CGT crystal does not uniformly switch magnetization, but rather responds to the external applied field by continuous domain formation [35].

B. History dependence of magnetic spin textures

The investigated CGT flake, shown in Fig. 1(d), is 40 nm thick, while the triangular shaped region (slight gray contrast) toward the upper end of the flake has a total thickness of 55 nm [36]. The XMCD image of the flake in Fig. 1(e), where the gray scale is directly proportional to the out-of-plane magnetization, was obtained as the difference between two STXM images acquired with circular positive polarization and opposite saturated magnetization (+250 mT vs -250 mT). The XMCD signal testifies the ferromagnetic character of the flake, with the thicker region (triangle) displaying a larger XMCD signal.

The magnetization state of materials can significantly depend on the sample history, in particular the magnetic field and temperature evolution. Examples include $\text{Fe}_{1-x}\text{CoSi}$ whose magnetic behavior depends on the cooling protocol [37], the formation of specific magnetic phases in $\text{Ni}_{45}\text{Co}_5\text{Mn}_{38}\text{Sn}_{12}$ [38], the formation of metastable spin- and charge-ordered states, which in some cases have near-infinite lifetimes [39], as well as the metastable skyrmion formation in MnSi and Cu_2OSeO_3 [40,41]. A history dependence of the magnetic phase diagram has also been documented for thin film systems with Dzyaloshinskii-Moriya interaction (DMI)-stabilized skyrmions [42] or 2D magnets like FGT [25]. Other systems show less history-dependent spin textures such as $\text{La}_{1-x}\text{Sr}_x\text{MnO}_3$ which hosts dipolar stabilized magnetic textures [43].

In general, the magnetic phase diagram of CGT is comprised of regions exhibiting uniform magnetization (u), skyrmion (sks), and stripe domain (sd) states, and features the different magnetic spin textures obtained for the different manipulation protocols, i.e., the field-sweep (FS), field-cooling (FC), and zero-field cooling (ZFC) protocol. For the present CGT flake, the magnetic phase diagram could be determined from the negative to positive saturated state and temperatures between 25 K and 45 K, where the lower limit is determined by the cryogenic system of the end station, and the upper limit by the low magnetic contrast close to the Curie temperature of CGT.

1. Field-sweep measurements

An exemplary image series obtained following the FS procedure is presented in Figs. 3(a)–3(h) [44]. Starting from uniform magnetization at -70 mT and 30 K in Fig. 3(b), magnetic stripes (dark) begin to form. With increasing magnetic field, the size of the bright and dark domains becomes comparable at 0 mT, as expected for zero magnetization. Upon further increasing the field, the dark domains expand until only very sparse bright domains are visible at 80 mT. At highest magnetic field, uniform magnetization is reached [Fig. 3(h)].

In Fig. 3(a), the boundary between the 40 nm thick part of the CGT flake and the 55 nm thick triangular-shaped region is marked by a dashed white line. The formation of stripe domains occurs at lower field in the thicker region compared to the thinner region, which can be seen in Figs. 3(b) and 3(g). Further information can be gained by comparing the domain periodicity in the two regions for the 0 mT state at a specific temperature. To this end, more than ten representative

stripe periodicities were manually evaluated and averaged. Interestingly, the thinner region exhibits a significantly smaller domain periodicity in comparison to the thicker region (97 nm vs 120 nm), which is qualitatively visible in Fig. 3(d). Kittel's formula for domain size predicts that the stripe domain periodicity should decrease with decreasing sample thickness. However, when approaching the few layer limit, this formula no longer holds [45], and the domains are governed primarily by the balance between the exchange interaction and surface anisotropy [46,47], leading to an increase in the stripe size. In the present case, the thickness dependence indicates a regime where Kittel's formula holds. However, previous work on FGT flakes with a similar thickness showed larger domains for thinner regions [25]. It follows that the critical thickness depends on the specific parameters of the magnetic material, in particular the balance of exchange, magnetic anisotropy, and the dipolar interaction, and thus the domain size can be tuned.

While for the thicker region, the temperature dependence of the domain periodicity could be evaluated between 25 K and 45 K, for the thinner region this was possible only for 30 K and 35 K due to the lower contrast. The resulting plot in Fig. 3(i) reveals an increase of domain periodicity with decreasing temperature for both regions. For the thicker region, the domain periodicity is seen to increase from 110 nm at 45 K to 130 nm at 25 K. Such modulation by about 20% upon lowering the temperature by 20 K is small compared to that reported for FGT, in which case the periodicity increases by a factor of four (from 50 nm to 200 nm) over the same relative temperature range [25]. The different domain periodicity changes over the same absolute temperature interval, in conjunction with the significantly different Curie temperatures (195 K for FGT vs 70 K for CGT), signify differences in the properties of these 2D magnets. In particular, we speculate that the magnitude of the uniaxial anisotropy, and its temperature dependence, determines this behavior. For CGT, spatial mapping of the magnetization of a 100 nm thick flake patterned by focused ion beam revealed a domain width of about 290 nm [7]. This value is significantly larger than the present domain periodicity of 130 nm for the 55 nm thick CGT region at 25 K, which is most likely due to its smaller thickness.

The magnetic phase diagram obtained by the FS protocol, displayed in Figs. 3(j) and 3(k), reveals that for low temperatures, the magnetic state switches from negative saturation via stripe domains to positive saturation magnetization. Notably, at temperatures above 30 K, some of the bright stripe domains at positive field collapse into isolated skyrmions indicated by the light green color. The collapse into isolated skyrmions could be related to local pinning sites, although their identity and distribution remains a subject of further investigation. Compared to FGT [25], the CGT magnetic phase diagram exhibits a much smaller field asymmetry of the stripe domain phase.

2. Field-cooled measurements

In bulk chiral magnets [48] or 2D magnets such as FGT [25], a high temperature phase pocket exists, where the sample is entirely filled by a skyrmion lattice. In CGT, due to

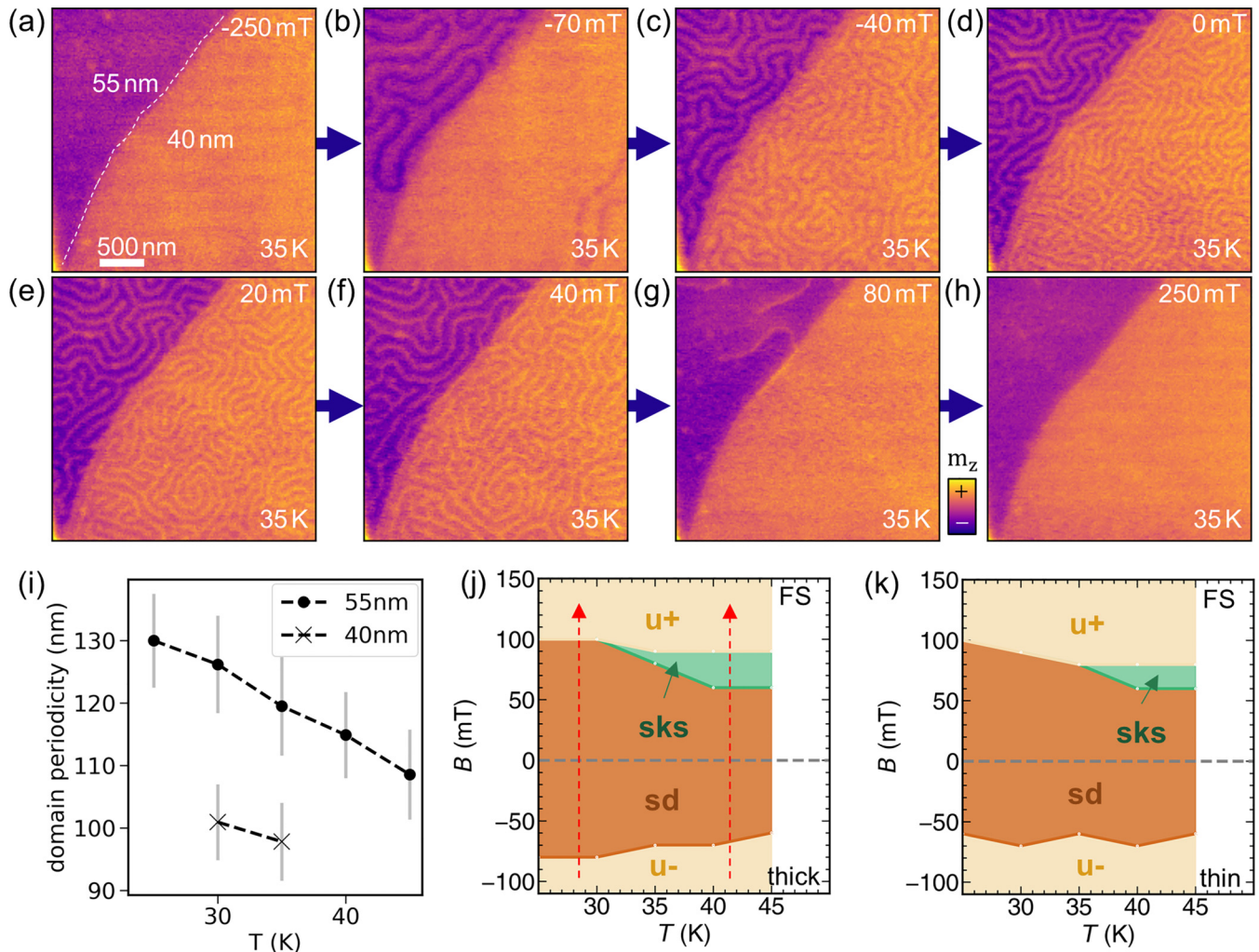


FIG. 3. Magnetic phases of the CGT flake induced by the field-sweep protocol. (a)–(h) STXM image series taken at 35 K at different magnetic fields as indicated. (i) Temperature dependence of magnetic domain periodicity at 0 mT for the two different flake thicknesses. Each data point belongs to the 0 mT STXM image of the series. The vertical gray lines indicate the standard deviation. (j), (k) Field-sweep magnetic phase diagram obtained for the (j) thicker (55 nm) and (k) thinner (40 nm) flake region, with uniform magnetization (u), stripe domains (sd), and skyrmions (sks). The dashed red arrows in panel (j) indicate the performed field sweeps.

the low magnetic contrast, we could not directly probe this temperature region (above 45 K). However, in some cases it is also possible to stabilize skyrmions outside of this region by cooling the sample under an applied magnetic field (field cooling, FC) through the equilibrium pocket, resulting in the formation of metastable skyrmions at lower temperatures. In this manner, skyrmions can be realized at temperatures where they otherwise would not form by, e.g., field sweeping. Figures 4(a)–4(h) display an exemplary series of STXM images obtained following the FC protocol, achieved after field cooling at 20 mT from 70 K to 30 K, which resulted in the formation of a dense array of skyrmions [49]. This observation hints toward the presence of a high temperature skyrmion phase pocket in CGT, where a dense skyrmion lattice could presumably be realized.

Following the initial FC, we acquired images for both decreasing and increasing applied magnetic field in two separate measurement runs. Upon decreasing the magnetic field, it is evident that the size of the skyrmions increased, and they started to merge with adjacent skyrmions into stripe-shaped

configurations [see Fig. 4(c)]. The resulting domain network then contracted into a looplike, loose network of (dark) domains [Fig. 4(d)] before the uniformly magnetized state was finally reached. By contrast, application of a magnetic field opposite to the core of the skyrmions primarily decreased the skyrmion size, as apparent from Figs. 4(e)–4(h). This trend is similar to that recently observed on CGT before its transition to the uniformly magnetized state at 100 mT [7]. In that work, Bloch domain walls were investigated while probing the in-plane field dependence of the spin textures. The significant size change of the skyrmions with magnetic field testifies that the dipolar interaction plays a significant role in their stabilization [50].

We were able to probe the field extent of the high temperature skyrmion phase by field cooling at a range of different applied magnetic fields, as shown in Figs. 4(i)–4(k). While at 40 mT, a high density of skyrmions is formed, FC at 60 mT leads to fewer skyrmions and partially striped domains. In contrast, FC at 80 mT does not yield any spin texture, indicating that the upper bound of the skyrmion phase pocket

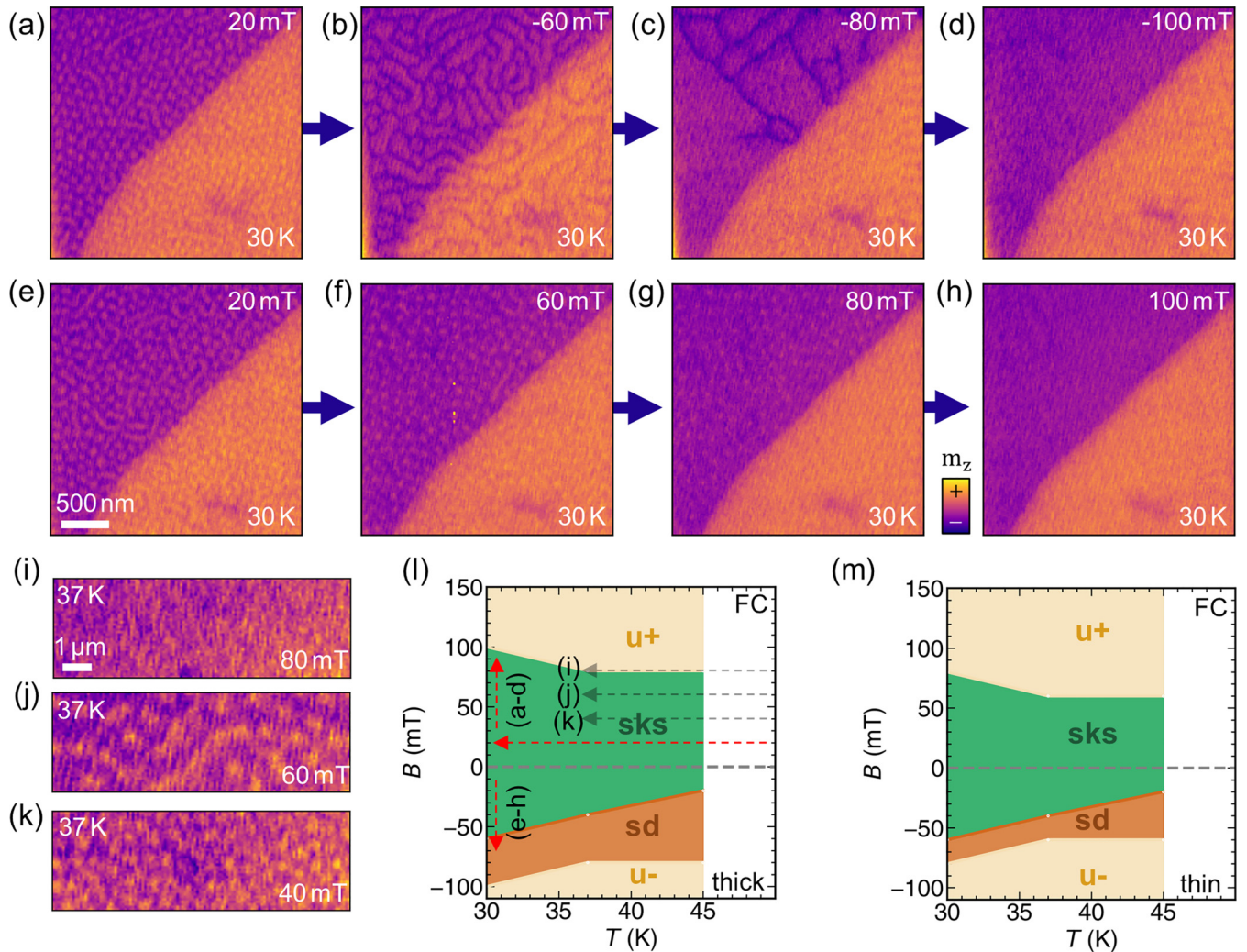


FIG. 4. Magnetic phases of the CGT flake induced by field-cooling. (a)–(d) Series of STXM images acquired upon stepwise decreasing the magnetic field applied to a skyrmion lattice prepared by field cooling to 30 K at 20 mT. (e)–(h) Corresponding series of STXM images obtained upon changing the magnetic field in opposite direction. (i)–(k) STXM images of the thicker flake region recorded upon field cooling under different magnetic fields to 37 K. (l), (m) Field-cooled magnetic phase diagrams for the two different flake thicknesses, with the dashed arrows indicating the paths for field cooling [red arrows belong to panels (a)–(h), gray arrows to panels (i)–(k)].

is located between 60 mT and 80 mT. These different FC procedures are indicated in the magnetic phase diagrams for the thick and thin flake region in Figs. 4(l) and 4(m), respectively. The phase diagrams show that skyrmions exist down to low temperatures, even with a slight stability increase for the lowest measured temperature at positive magnetic fields compared to higher temperatures. For negative magnetic fields, the skyrmions transform into a stripe domain network which expands to more negative fields at lower temperatures. Comparison between the two phase diagrams in Figs. 4(l) and 4(m) reveals that the spin textures of the thinner flake region persist down to lower absolute magnetic fields, as compared to the thicker one.

3. Zero-field cooled measurements

Very recently, it has been observed that ZFC of FGT flakes can induce the formation of higher-order spin textures, namely composite skyrmions [20]. In its simplest version, a composite

skyrmion is a superposition of two skyrmions of opposite polarity, which has also been termed skyrmionium [51]. As this superposition leads to an overall topological charge of zero, its stabilization cannot be of topological nature. In STXM images, a skyrmionium appears as a ring-shaped object of out-of-plane magnetization. Previously, higher-order spin textures have also been observed in a ferromagnet/magnetic topological insulator heterostructure or B20 chiral magnets [52,53].

A suitable protocol to induce such higher-order spin textures starts with ZFC of the sample to temperatures well below the Curie temperature, in order to prepare closed magnetic domain loops, which eventually will collapse into isolated magnetic objects upon sweeping the magnetic field. Figures 5(a)–5(h) show the magnetic field evolution of such a ZFC magnetic state in the CGT flake, featuring the formation of closed loops [54]. Moreover, a small skyrmionium can be discerned in Fig. 5(g). A zoom into another observed skyrmionium with a lateral size on the order of 500 nm is shown in

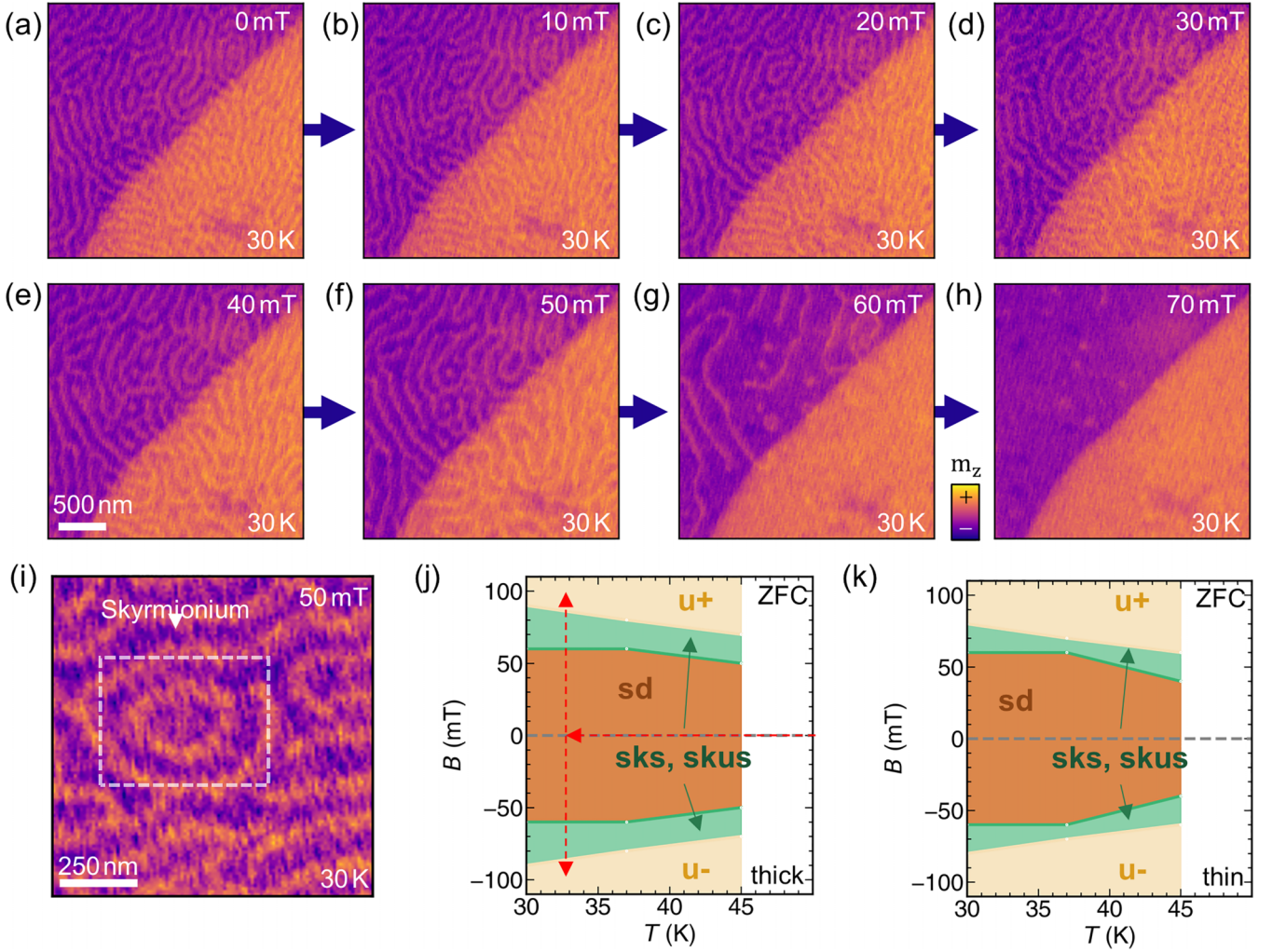


FIG. 5. Magnetic phases of the GGT flake induced by zero-field cooling. (a)–(h) STXM image series starting from the zero-field cooled magnetic state at 30 K. (i) STXM image of a skyrmionium formed at 30 K after increasing the magnetic field to 50 mT. (j), (k) Zero-field cooled magnetic phase diagrams for the two different flake thicknesses with uniform magnetization (u), stripe domains (sd), skyrmions (sks), and skyrmioniums (skus).

Fig. 5(i). The conditions under which skyrmioniums evolve in CGT are similar to those previously reported for skyrmionium formation in FGT [20], suggesting a similar underlying formation mechanism. It involves thermal fluctuations at the critical temperature in absence of external magnetic field, which leads to the formation of doubly enclosed domain walls that are needed for the formation of skyrmioniums. While standard STXM does not allow the resolution of the in-plane structure of skyrmioniums, it should be noted that LTEM enables detecting the formation of bubbles of different topologies in CGT flakes [7,8].

By ZFC the CGT flake to different temperatures and repeating the magnetic field series, ZFC magnetic phase diagrams were determined, as shown in Figs. 5(j) and 5(k). It is evident that at lower fields, stripe domains dominate, whereas at higher fields skyrmioniums and skyrmions coexist together with residual stripes. For both flake thicknesses, the stability of the spin textures is enhanced at lower temperatures, while the magnetic field-related stability range is narrower for the thinner region, in accordance with the FS and FC phase diagrams in Figs. 3 and 4.

IV. SUMMARY AND CONCLUSION

In summary, our analysis of the magnetic phase diagram of a CGT flake has shown that the temperature-dependent domain periodicity decreases with decreasing flake thickness. In addition, indirect evidence could be gained for the existence of a high-temperature skyrmion phase pocket in CGT. The pronounced sensitivity of the field-cooled skyrmions to changes in the magnetic field indicates that dipolar interactions play a major role in their stabilization, rather than a significant DMI. Moreover, we found that skyrmioniums can be nucleated in CGT upon ZFC and subsequent magnetic field ramping, which complements the previously reported formation of composite skyrmions in FGT, and reaffirms the general nature of the formation mechanism. This highlights the possibility to unravel further, higher-order spin textures with potential applications in 2D spintronics. Taken together, the presented results underscore the potential of CGT for 2D spintronic applications, ranging from nonvolatile magnetic random-access memories (MRAMs) [55] to devices that exploit local spin textures such as skyrmions or skyrmioniums [56] to neuromorphic spintronics [57], where the

implementation of skyrmions may help to achieve a continuous tuning of weights [12].

ACKNOWLEDGMENTS

The authors thank the Helmholtz-Zentrum Berlin for the allocation of synchrotron beamtime as well as Jürgen Weis,

Ulrike Waizmann, Achim Güth, Thomas Reindl, and Marion Hagel at the Nanostructuring Lab (NSL) of the MPI for Solid State Research for technical support. M.B. is grateful for support by the Deutsche Forschungsgemeinschaft (DFG) through SPP-2244 “2D Materials - Physics of van der Waals [hetero]structures” via Grant BU 1125/12-1.

-
- [1] C. Gong, L. Li, Z. Li, H. Ji, A. Stern, Y. Xia, T. Cao, W. Bao, C. Wang, Y. Wang *et al.*, *Nature (London)* **546**, 265 (2017).
- [2] D. Edelberg, D. Rhodes, A. Kerelsky, B. Kim, J. Wang, A. Zangiabadi, C. Kim, A. Abhinandan, J. Ardelean, M. Scully, D. Scullion, L. Embon, R. Zu, E. J. G. Santos, L. Balicas, C. Marianetti, K. Barmak, X. Zhu, J. Hone, and A. N. Pasupathy, *Nano Lett.* **19**, 4371 (2019).
- [3] A. Bedoya-Pinto, J.-R. Ji, A. K. Pandeya, P. Gargiani, M. Valvidares, P. Sessi, J. M. Taylor, F. Radu, K. Chang, and S. S. P. Parkin, *Science* **374**, 616 (2021).
- [4] Y. Deng, Y. Yu, Y. Song, J. Zhang, N. Z. Wang, Z. Sun, Y. Yi, Y. Z. Wu, S. Wu, J. Zhu *et al.*, *Nature (London)* **563**, 94 (2018).
- [5] M. Gibertini, M. Koperski, A. F. Morpurgo, and K. S. Novoselov, *Nat. Nanotechnol.* **14**, 408 (2019).
- [6] S. Manipatruni, D. E. Nikonov, C.-C. Lin, T. A. Gosavi, H. Liu, B. Prasad, Y.-L. Huang, E. Bonturim, R. Ramesh, and I. A. Young, *Nature (London)* **565**, 35 (2019).
- [7] M.-G. Han, J. A. Garlow, Y. Liu, H. Zhang, J. Li, D. DiMarzio, M. W. Knight, C. Petrovic, D. Jariwala, and Y. Zhu, *Nano Lett.* **19**, 7859 (2019).
- [8] A. R. McCray, Y. Li, E. Qian, Y. Li, W. Wang, Z. Huang, X. Ma, Y. Liu, D. Y. Chung, M. G. Kanatzidis *et al.*, *Adv. Funct. Mater.* **33**, 2214203 (2023).
- [9] C. Back, V. Cros, H. Ebert, K. Everschor-Sitte, A. Fert, M. Garst, T. Ma, S. Mankovsky, T. Monchesky, M. Mostovoy *et al.*, *J. Phys. D* **53**, 363001 (2020).
- [10] D. Feng, Z. Shen, Y. Xue, Z. Guan, R. Xiao, and C. Song, *Nanoscale* **15**, 1561 (2023).
- [11] W. Kang, Y. Huang, X. Zhang, Y. Zhou, and W. Zhao, *Proc. IEEE* **104**, 2040 (2016).
- [12] K. M. Song, J.-S. Jeong, B. Pan, X. Zhang, J. Xia, S. Cha, T.-E. Park, K. Kim, S. Finizio, J. Raabe *et al.*, *Nat. Electron.* **3**, 148 (2020).
- [13] Y. Wu, B. Francisco, Z. Chen, W. Wang, Y. Zhang, C. Wan, X. Han, H. Chi, Y. Hou, A. Lodesani *et al.*, *Adv. Mater.* **34**, 2110583 (2022).
- [14] W. Liu, Y. Wang, Y. Han, W. Tong, J. Fan, L. Pi, N. Hao, L. Zhang, and Y. Zhang, *J. Phys. D* **53**, 025101 (2020).
- [15] S. Selter, G. Bastien, A. U. B. Wolter, S. Aswartham, and B. Büchner, *Phys. Rev. B* **101**, 014440 (2020).
- [16] I. A. Verzhbitskiy, H. Kurebayashi, H. Cheng, J. Zhou, S. Khan, Y. P. Feng, and G. Eda, *Nat. Electron.* **3**, 460 (2020).
- [17] W. Zhuo, B. Lei, S. Wu, F. Yu, C. Zhu, J. Cui, Z. Sun, D. Ma, M. Shi, H. Wang *et al.*, *Adv. Mater.* **33**, 2008586 (2021).
- [18] W. Xing, Y. Chen, P. M. Odenthal, X. Zhang, W. Yuan, T. Su, Q. Song, T. Wang, J. Zhong, S. Jia *et al.*, *2D Mater.* **4**, 024009 (2017).
- [19] K. Wang, T. Hu, F. Jia, G. Zhao, Y. Liu, I. V. Solovyev, A. P. Pyatakov, A. K. Zvezdin, and W. Ren, *Appl. Phys. Lett.* **114**, 092405 (2019).
- [20] L. Powalla, M. T. Birch, K. Litzius, S. Wintz, F. S. Yasin, L. A. Turnbull, F. Schulz, D. A. Mayoh, G. Balakrishnan, M. Weigand, X. Yu, K. Kern, G. Schütz, and M. Burghard, *Adv. Mater.* **35**, 2208930 (2023).
- [21] Cr₂Ge₂Te₆ crystal structure: Datasheet in springermaterials, (accessed 2023-04-11), copyright 2016 Springer-Verlag Berlin Heidelberg & Material Phases Data System (MPDS), Switzerland & National Institute for Materials Science (NIMS), Japan
- [22] M. Weigand, S. Wintz, J. Gräfe, M. Noske, H. Stoll, B. Van Waeyenberge, and G. Schütz, *Crystals* **12**, 1029 (2022).
- [23] See Supplemental Material at <http://link.aps.org/supplemental/10.1103/PhysRevB.108.214417> for x-ray spectra at the Cr-L3-edge (Supp Fig S1a,b).
- [24] M. Weigand, *Realization of a New Magnetic Scanning X-Ray Microscope and Investigation of Landau Structures under Pulsed Field Excitation* (Cuvillier Verlag, Göttingen, 2015).
- [25] M. Birch, L. Powalla, S. Wintz, O. Hovorka, K. Litzius, J. Loudon, L. Turnbull, V. Nehruji, K. Son, C. Bubeck *et al.*, *Nat. Commun.* **13**, 3035 (2022).
- [26] L. Powalla, M. T. Birch, K. Litzius, S. Wintz, F. Schulz, M. Weigand, T. Scholz, B. V. Lotsch, K. Kern, G. Schütz *et al.*, *Nano Lett.* **22**, 9236 (2022).
- [27] See Supplemental Material at <http://link.aps.org/supplemental/10.1103/PhysRevB.108.214417> for exemplary STXM images with magnetic contrast, the saturated state and the calculated difference image using background subtraction (Supp Fig S1c-e).
- [28] V. Carreaux, D. Brunet, G. Ouvrard, and G. Andre, *J. Phys.: Condens. Matter* **7**, 69 (1995).
- [29] X. Zhang, Y. Zhao, Q. Song, S. Jia, J. Shi, and W. Han, *Jpn. J. Appl. Phys.* **55**, 033001 (2016).
- [30] Y. Liu, C. Petrovic *et al.*, *Phys. Rev. B* **96**, 054406 (2017).
- [31] T. M. Project, Data retrieved from the Materials Project for Cr-GeTe3 (mp-541449) from database version v2023.11.1, <https://next-gen.materialsproject.org/materials/mp-541449>.
- [32] A. Jain, S. P. Ong, G. Hautier, W. Chen, W. D. Richards, S. Dacek, S. Cholia, D. Gunter, D. Skinner, G. Ceder *et al.*, *APL Mater.* **1**, 011002 (2013).
- [33] M. Sato and Y. Ishii, *J. Appl. Phys.* **66**, 983 (1989).
- [34] N. Richter, D. Weber, F. Martin, N. Singh, U. Schwingenschlögl, B. V. Lotsch, and M. Kläui, *Phys. Rev. Mater.* **2**, 024004 (2018).
- [35] T. Guo, Z. Ma, X. Luo, Y. Hou, W. Meng, J. Wang, J. Zhang, Q. Feng, G. Lin, Y. Sun *et al.*, *Mater. Character.* **173**, 110913 (2021).
- [36] See Supplemental Material at <http://link.aps.org/supplemental/10.1103/PhysRevB.108.214417> for AFM measurements (Supp Fig S2).
- [37] A. Bauer, M. Garst, and C. Pfleiderer, *Phys. Rev. B* **93**, 235144 (2016).

- [38] A. Banerjee, P. Chaddah, S. Dash, K. Kumar, A. Lakhani, X. Chen, and R. V. Ramanujan, *Phys. Rev. B* **84**, 214420 (2011).
- [39] F. Kagawa and H. Oike, *Adv. Mater.* **29**, 1601979 (2017).
- [40] H. Oike, A. Kikkawa, N. Kanazawa, Y. Taguchi, M. Kawasaki, Y. Tokura, and F. Kagawa, *Nat. Phys.* **12**, 62 (2016).
- [41] A. Chacon, L. Heinen, M. Halder, A. Bauer, W. Simeth, S. Mühlbauer, H. Berger, M. Garst, A. Rosch, and C. Pfleiderer, *Nat. Phys.* **14**, 936 (2018).
- [42] N. K. Duong, M. Raju, A. Petrović, R. Tomasello, G. Finocchio, and C. Panagopoulos, *Appl. Phys. Lett.* **114**, 072401 (2019).
- [43] A. Kotani, H. Nakajima, K. Harada, Y. Ishii, and S. Mori, *Phys. Rev. B* **95**, 144403 (2017).
- [44] See Supplemental Material at <http://link.aps.org/supplemental/10.1103/PhysRevB.108.214417> for extended data for image series obtained following the FS procedure (Supp Fig S3 and S4).
- [45] Z. Málek and V. Kamberský, *Czechoslovakij fiziceskij zurnal* **8**, 416 (1958).
- [46] B. Kaplan and G. Gehring, *J. Magn. Magn. Mater.* **128**, 111 (1993).
- [47] Y. Yafet and E. M. Gyorgy, *Phys. Rev. B* **38**, 9145 (1988).
- [48] L. J. Bannenberg, H. Wilhelm, R. Cubitt, A. Labh, M. P. Schmidt, E. Lelièvre-Berna, C. Pappas, M. Mostovoy, and A. O. Leonov, *npj Quantum Mater.* **4**, 11 (2019).
- [49] See Supplemental Material at <http://link.aps.org/supplemental/10.1103/PhysRevB.108.214417> for extended data for image series obtained following the FC procedure (Supp Fig S5).
- [50] F. Büttner, I. Limesh, and G. S. Beach, *Sci. Rep.* **8**, 4464 (2018).
- [51] B. Göbel, A. F. Schäffer, J. Berakdar, I. Mertig, and S. S. Parkin, *Sci. Rep.* **9**, 12119 (2019).
- [52] J. Tang, Y. Wu, W. Wang, L. Kong, B. Lv, W. Wei, J. Zang, M. Tian, and H. Du, *Nat. Nanotechnol.* **16**, 1086 (2021).
- [53] S. Zhang, F. Kronast, G. van der Laan, and T. Hesjedal, *Nano Lett.* **18**, 1057 (2018).
- [54] See Supplemental Material at <http://link.aps.org/supplemental/10.1103/PhysRevB.108.214417> for extended data for image series obtained following the ZFC procedure (Supp Fig S6).
- [55] H. Yang, S. O. Valenzuela, M. Chshiev, S. Couet, B. Dieny, B. Dlubak, A. Fert, K. Garello, M. Jamet, D.-E. Jeong *et al.*, *Nature (London)* **606**, 663 (2022).
- [56] C. Marrows and K. Zeissler, *Appl. Phys. Lett.* **119**, 250502 (2021).
- [57] J. Grollier, D. Querlioz, K. Camsari, K. Everschor-Sitte, S. Fukami, and M. D. Stiles, *Nat. Electron.* **3**, 360 (2020).